Background rates of x-ray transition-edge sensor micro-calorimeters under a frequency domain multiplexing readout for solar axion-like particles' detection

Vaccaro, D.; Gottardi, L.; Akamatsu, H.; van der Kuur, J.; Nagayoshi, K.; Taralli, E.; de Wit, M.; Ravensberg, K.; Gao, J. R.; den Herder, J. W.A.

DOI
10.1063/5.0142367

Publication date
2023

Document Version
Final published version

Published in
Review of Scientific Instruments

Review of Scientific Instruments ARTICLE scitation.org/journal/rsi

Background rates of x-ray transition-edge sensor micro-calorimeters under a frequency domain multiplexing readout for solar axion-like particles' detection

Cite as: Rev. Sci. Instrum. 94, 043104 (2023); doi: 10.1063/5.0142367
Submitted: 13 January 2023 • Accepted: 31 March 2023 •
Published Online: 21 April 2023

D. Vaccaro,[1,a] L. Gottardi,[1] H. Akamatsu,[1] J. van der Kuur,[2] K. Nagayoshi,[1] E. Taralli,[1] M. de Wit,[1] K. Ravensberg,[1] J. R. Gao,[1,3] and J. W. A. den Herder[1,4]

AFFILIATIONS

[1] NWO-I/SRON Netherlands Institute for Space Research, Niels Bohrweg 4, 2333 CA Leiden, The Netherlands
[2] NWO-I/SRON Netherlands Institute for Space Research, Landleven 12, 9747 AD Groningen, The Netherlands
[3] Optics Group, Department of Imaging Physics, Delft University of Technology, Delft 2628 CJ, The Netherlands
[4] Universiteit van Amsterdam, Science Park 904, 1090 GE Amsterdam, The Netherlands

[a] **Author to whom correspondence should be addressed:** d.vaccaro@sron.nl

ABSTRACT

We report on the x-ray background rate measured with transition-edge sensors (TES) micro-calorimeters under frequency-domain multiplexing (FDM) readout as a possible technology for future experiments aiming at a direct detection of axion-like particles. Future axion helioscopes will make use of large magnets to convert axions into photons in the keV range and x-ray detectors to observe them. To achieve this, a detector array with high spectral performance and extremely low background is necessary. TES are single-photon, non-dispersive, high-resolution micro-calorimeters and represent a possible candidate for this application. We have been developing x-ray TES micro-calorimeters and an FDM readout technology in the framework of the space-borne x-ray astronomical observatories. We show that the current generation of our detectors is already a promising technology for a possible axion search experiment, having measured an x-ray background rate of $2.2(2) \times 10^{-4}$ cm^{-2} s^{-1} keV^{-1} with a cryogenic demonstrator not optimized for this specific application. We then make a prospect to further improve the background rate down to the required value ($<10^{-7}$ cm^{-2} s^{-1} keV^{-1}) for an axion-search experiment, identifying no fundamental limits to reach such a level.

I. INTRODUCTION

Many future experiments aiming at scientific breakthroughs in the fields of astronomy, cosmology, and nuclear and particle physics will employ large arrays of cryogenic detectors, such as metallic-magnetic calorimeters (MMC)[1] or transition-edge sensors (TES).[2] In particular, TESs are employed as detector technology in a number of future satellite observatories (ESA's Athena x-ray Integral Field Unit,[3] CNSA's Hot Universe Baryon Surveyor,[4] and JAXA's Lite-BIRD[5]) as well as Earth-based experiments for the direct search for dark matter,[6] direct neutrino mass measurements,[7] or searches for neutrino-less double beta decay.[8] Furthermore, TES arrays could find potential ground-based applications in the study of hot plasma for nuclear fusion research,[9] in material analysis,[10] and in the direct detection of solar axions.[11]

Axions or axion-like particles (ALPs) are hypothetical, weakly interacting pseudo-scalar particles originally introduced as a solution to the strong CP problem.[12] In more recent times, ALPs have become an attractive dark matter candidate.[13] According to the theory,[14] axions possess a coupling to photons, parameterized by a coupling constant $g_{a\gamma}$, which can be exploited to facilitate the conversion of the axion into photons inside a magnetic field. This idea is at the basis of axion helioscopes,[15] which aim at detecting the ALP flux generated in the Sun from Primakoff conversion and processes involving electrons in a plasma.[16]

An axion helioscope essentially consists of a large magnet of length L and field intensity B pointed toward the Sun, with the field aligned in the transverse direction, where axions would convert into photons in the keV range. The number of conversions depends on the axion flux and the conversion probability, which for axion masses $m_a < 10$ meV is[16]

$$P_{a\to\gamma} \simeq g_{a\gamma}^2 B^2 L^2/4. \quad (1)$$

The CERN axion solar telescope (CAST)[17] has set the best limit to date on $g_{a\gamma}$ at 6.6×10^{-11} GeV^{-1}. Its successor, the International AXion Observatory (IAXO),[18] will offer the possibility to lower this limit by at least one order of magnitude. BabyIAXO,[19] the prototype stage of this experiment, will employ a 10 m long magnet with an average magnetic field intensity of 2.5 T.

For such applications, the employment of x-ray detectors with an extremely low background is required (<10^{-7} cm^{-2} s^{-1} keV^{-1} for BabyIAXO). The ideal x-ray detector for an axion helioscope should also have a high quantum efficiency, low energy threshold, and easiness of readout. TES micro-calorimeters offer an attractive combination of such characteristics, making them a suitable choice for this application. An additional feature of TES arrays is the possibility of a large active area, although at the present status of the detector concept in Baby-IAXO, a large detection area is not beneficial.

Moreover, a high spectral resolution at the eV level is a desirable feature to be able to resolve the fine structures in the solar axion spectrum in the case of detection,[20] which would allow us to study in more detail the underlying physics. This feature can only be granted by cryogenic detectors, such as TES or MMC. For comparison, Micromegas detectors demonstrated resolving power capabilities $\Delta E/E$ of the order of 20% at $E = 6$ keV,[21] whereas at SRON, we have shown resolving powers for TES micro-calorimeters at a level of 0.03%.[22] A review of the detectors currently considered for IAXO is reported in Ref. 19.

In this paper, we report on the background rate measured for a TES array test chip developed at SRON. The paper is structured as follows: in Sec. II, we outline the fundamental concepts for TES and frequency domain multiplexing (FDM) readout; in Sec. III, we describe the experimental setup; in Sec. IV, we describe the experimental method and data analysis and discuss the results; and finally, in Sec. VI, we summarize our results and prospect future developments.

II. FUNDAMENTALS OF TES AND FDM READOUTS

A TES is composed of a superconducting film strongly coupled to a radiation absorber and weakly linked to a thermal bath at a temperature $T_b < T_C$, where T_C is the critical temperature of the film, typically at a level of 100 mK. TESs are used as extremely sensitive thermometers, by exploiting the sharp phase transition of the superconducting film. Under stiff voltage bias (either ac or dc), the TES is heated to its T_C, and stable operation is granted by the so-called negative electro-thermal feedback (ETF) mechanism. The observable signal is the TES current, which is typically amplified at the cryogenic stage by a Superconducting QUantum Interference Device (SQUID).

The fundamental quantities to parameterize the TES and its response to an incoming x-ray photon are[23]

$$\alpha \equiv \frac{T_0}{R_0}\frac{\partial R}{\partial T}\bigg|_{I_0} \quad \text{Temperature responsivity,} \quad ((2))$$

$$\mathscr{L} = \frac{P_0\alpha}{GT_0} \quad \text{ETF loop gain,} \quad ((3))$$

$$\tau = \frac{C}{G(1+\mathscr{L})} \quad \text{Effective time constant,} \quad ((4))$$

$$\Delta E_{FWHM} \simeq 2.355\sqrt{\frac{4k_B T_0^2 C}{\alpha}} \quad \text{Energy resolution,} \quad ((5))$$

where R, I, T, and P are the TES resistance, current, temperature, and power, respectively, and the subscript 0 denotes the values at the quiescent point, G and C are the TES thermal conductance and heat capacity, respectively, and k_B is the Boltzmann constant.

For micro-calorimeters, the energy resolution is the typical figure of merit for the detector performance. As can be seen from Eq. (5), to obtain high-resolving powers, it is desirable to have large temperature responsivity, low heat capacity, and low temperature. To avoid the detector saturation in the energy band of interest, these values are chosen as a trade-off between energy resolution and the detector dynamic range, which scales as C/α.

At SRON, we are developing x-ray TES micro-calorimeters for the backup detector array of Athena X-IFU, aiming to detect photons with energies ranging from 200 eV to 12 keV with a spectral resolution of 2.5 eV for energies up to 7 keV. In recent years, we have fabricated and tested several TES designs (in Fig. 1, we show an example) to match the required specifications for X-IFU and FDM readouts, demonstrating excellent energy resolutions for each design under ac-bias at the levels of $\Delta E_{FWHM} \approx 1.8$ eV or better for 6 keV photons.[22,24]

Typically, experiments employ arrays of a few thousands of TESs: to minimize the harness complexity and the thermal load at the cold stage where the detectors are mounted, a multiplexing readout scheme is necessary. Several multiplexing schemes exist, the most common ones being time-domain multiplexing[25] (TDM) and frequency-domain multiplexing[26] (FDM), where the TES is provided dc-bias and ac-bias, respectively. At SRON, we are developing the FDM readout technology for TES-based micro-calorimeters and bolometers with a base-band feedback scheme.[27]

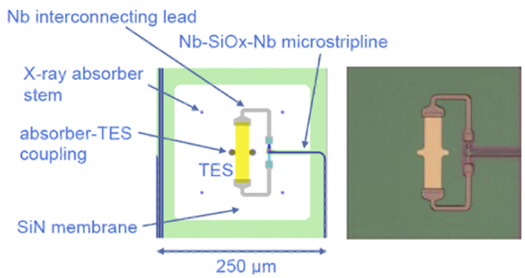

FIG. 1. Scheme for a high-aspect ratio TES designed at SRON and a microscope picture in false colors of the actual device, before the Au absorber deposition (therefore, stems are not yet visible).

In the FDM scheme, the detectors are voltage biased with a comb of sinusoidal carriers at different frequencies in the MHz range. Each TES is put in a series with a tuned, high-Q LC band-pass filter to limit the information bandwidth and allow only one carrier from the comb to provide the bias. To keep the same electrical bandwidth across the resonators, the inductance is kept constant and the frequencies are tuned by changing the capacitance. The TESs signals are then summed at the input coil of a SQUID and demodulated by room-temperature electronics. The base-band feedback nulls the signal at the SQUID by feeding back to the SQUID feedback coil the sum of the TES signals after a phase compensation.

We recently reported on the technological demonstration of our FDM technology, showing the simultaneous readouts of 31 and 37 pixels with two different cryogenic setups, with a summed spectral performance at 6 keV of 2.14 ± 0.03 and 2.23 ± 0.03 eV, respectively.[28]

III. DESCRIPTION OF THE SETUP

We conducted our experiments using one of our cryogenic FDM demonstrators, shown in Fig. 2, whose performance has been reported in Ref. 28. A schematic representation of the FDM readout is provided in Fig. 3.

The setup hosts an 8×8 TES array. Each TES consists of a Ti/Au bilayer of dimensions 80×13 μm^2, deposited on a 500 nm thick SiN membrane. The bilayer is coupled to a 240×240 μm^2, 2.3 μm thick Au absorber ($C = 0.85$ pJ/K at 90 mK) via two central pillars, with four additional corner Au stems providing mechanical support. The pitch between pixels is 250 μm, making for a geometrical efficiency of about 92%. The TES have a normal resistance of $R_N \approx 155$ mΩ, $T_C \approx 83$ mK, and $G \approx 65$ pW/K. The thermalization of the TES chip is provided by Au wire bondings between the gold top array and the Cu holder. Two superconducting Helmholtz coils (not visible in the picture) are placed above and below the TES chip to allow magnetic field tuning.

For the FDM readout, the TESs are connected to custom superconducting LC filters and transformers to allow for tuning of the current flowing through the TES. The inductance is 4 μH, and the transformer coil ratio is 1:1.125 with a coupling constant of $k \approx 0.94$, making an effective inductance of ≈3.6 μH. The detectors are voltage biased via a 750 mΩ resistor and a capacitive divider with a 1:25 ratio, resulting in an effective shunt resistance of ≈1 mΩ.

As cryogenic amplifiers, we are using a two-stage SQUID system developed by VTT,[29] consisting of a six-loop first stage and 184×4-loop second stage SQUIDs. An RC high-frequency filter is implemented at the first-stage SQUID input coil to suppress electrical oscillations due to coupling between the SQUID

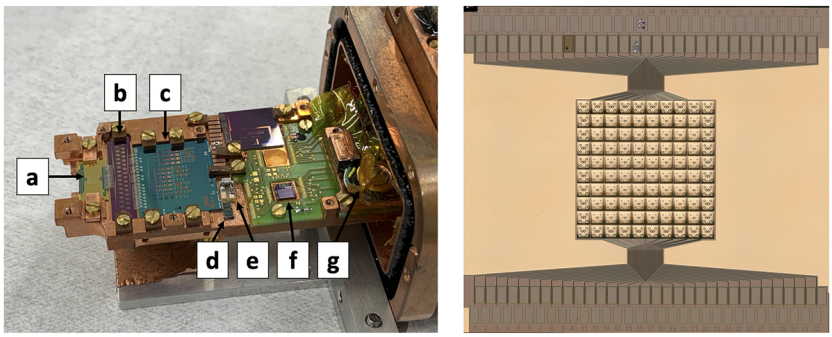

FIG. 2. (a) The cryogenic setup used for the measurements: (a) TES array, (b) transformers, (c) LC filters, (d) first-stage SQUID, (e) RC low-pass filter, (f) second-stage SQUID, and (g) Ge thermistor. (b) The microscope view of the TES array.

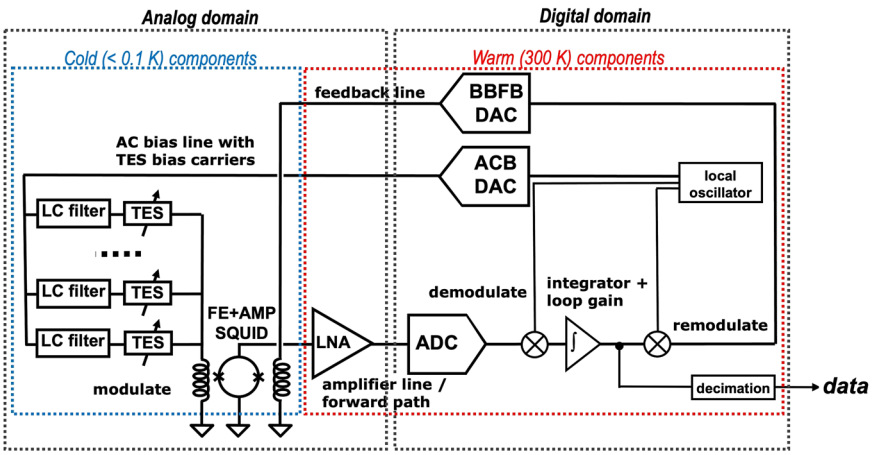

FIG. 3. The schematic representation of the FDM readout with base-band feedback.

input inductance and parasitics capacitance and inductance in the LC filter. SQUID control is handled at room temperature by an analog front-end electronics mounting a custom low-noise amplifier.

The cryogenic components are mounted on a custom holder made of oxygen-free high-conductivity (OFHC) copper and enclosed in an aluminum shield. To do spectral performance characterization, we typically use a ^{55}Fe source installed on the Al shield, producing x-rays at the Mn-Kα (5.90 keV) and Mn-Kβ (6.49 keV) lines. For calibration purposes, we employ also an external Modulated x-ray Source (MXS) generating photons at the lines of Cr-Kα (5.41 keV), Cr-Kβ (5.95 keV), Cu-Kα (8.05 keV), and Cu-Kβ (8.90 keV). During the acquisition of background data, the ^{55}Fe source was not installed.

The setup is hosted in a Leiden Cryogenics dilution refrigerator with a cooling power of 400 μW at 120 mK, where also three other cryogenic setups were mounted and active. The setups are suspended via Kevlar wires to the mixing chamber to dampen mechanical oscillations.[30] Thermal anchoring of the setup to the mixing chamber is ensured by OHFC copper braids and rods. The setup temperature is monitored via a Ge thermistor and regulated via a 500 Ω heater using a software PID loop. The temperature of the setup during the experiments reported in this paper was 56 mK.

The generation of the TESs bias voltages is modulated with ac carriers; the demodulation of the SQUID output signal and the re-modulation for base-band feedback are handled by a custom digital "DEMUX" board, mounting AD9724 DACs and a Xilinx XC7V585T Virtex 7 FPGA. Data are sampled at 20 Msps, and de-modulation is performed with a four-stage decimation filter down to 156.25 ksps.

IV. EXPERIMENTAL METHOD AND DATA ANALYSIS

In this section, we describe the procedure for the data acquisition, energy scale calibration, and data selection for the two experiments performed to estimate the background rate. The results, with and without passive shielding, are presented in Sec. V.

A. Data acquisition and online selection

To estimate the background rate of the detector array, the TES were biased on their working point at roughly 10% of the superconducting transition, where typically the best energy resolutions are observed. The TES currents were acquired simultaneously and continuously. Such continuous signals are divided into single traces of ≈105 ms (16 384 samples at 156.25 ksps). Data were stored in the form of binary files, each containing 2861 single traces per TES, i.e., 5 min of data acquisition. Due to the large rate of file volume being generated (≈80 GB/h), long-term storing of raw data was discarded for practical reasons. Hence, we employed an online data selection algorithm: in the same time as data for a new binary file was being acquired, noise events in the previously completed file were analyzed to search for background x-ray events.

The pulse shape for a 6 keV event is shown in Fig. 4. For the chosen working point on the TES transition, the values for the rise time and fall time constants are at a level of 100 μs and 1 ms, respectively.

For each trace, after baseline correction, an offline trigger was used to identify the possible events. The trigger level was defined with a 3σ detection threshold, as shown in the inset of Fig. 4, which is calculated as the root mean square of the TES baseline fluctuations. In the case of detection, the single trace is tagged as an x-ray event and stored in a different binary file, saving the event information for further offline analysis.

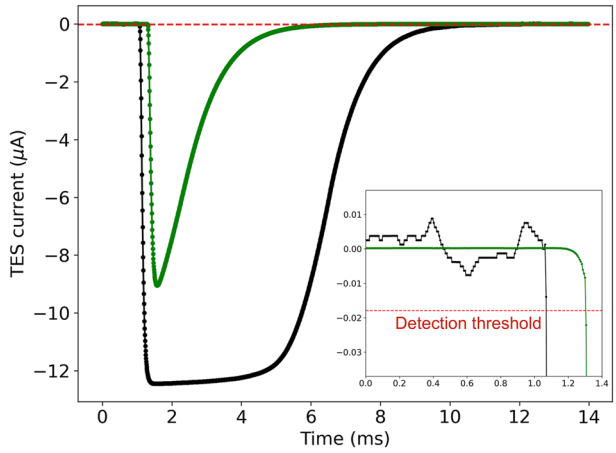

FIG. 4. The black line shows an example of a saturated pulse due to ≈35 keV released in the absorber. The dashed red line shows the 3σ threshold. The green line shows the 6 keV template built from the calibration data. The inset shows a zoom of the TES baseline current, right before the pulse rise, with respect to the 3σ detection threshold.

B. Energy scale calibration

To estimate the energy of the recorded pulses, we first calibrate the energy scale individually for each detector. To do so, we use the calibration spectra acquired using the ^{55}Fe source and the MXS (see Fig. 5). A template is generated by averaging the x-ray pulses from the Mn-Kα and Mn-Kβ lines and used to calibrate the spectrum using the optimal filtering technique.[31] The position of the different spectral lines can be estimated using histograms of the single event amplitudes derived with the optimal filter, by a fit with a Gaussian function.

Using the optimal filter fit to calibrate the energy scale, however, is not the best approach for this particular case. This is because our current TES arrays are designed for the energy range of X-IFU (0.2 to 12 keV) and the TES response saturates for x-ray pulses with energy above this value, as shown in Fig. 4. If the optimal filter fits were used as the parameters to estimate the energy of the x-ray photons, the energy of such saturated pulses would then be underestimated, as shown in Fig. 6.

However, even if the pulse is saturated, the integrated area of the pulse will still be proportional to the energy released in the TES absorber. Assuming that the deposited energy exceeds the detector dynamic range: the larger the energy deposited, the longer the TES will stay in a working point close to the normal state (i.e., $\alpha \approx 0$) because a longer time is needed for the heat to be dissipated toward the thermal bath. Therefore, the pulse shape will be saturated for a longer time, thus subtending a larger area.

Therefore, we choose to estimate the energy from the pulse area, or the surface, subtended by the x-ray pulse. In this way, we are

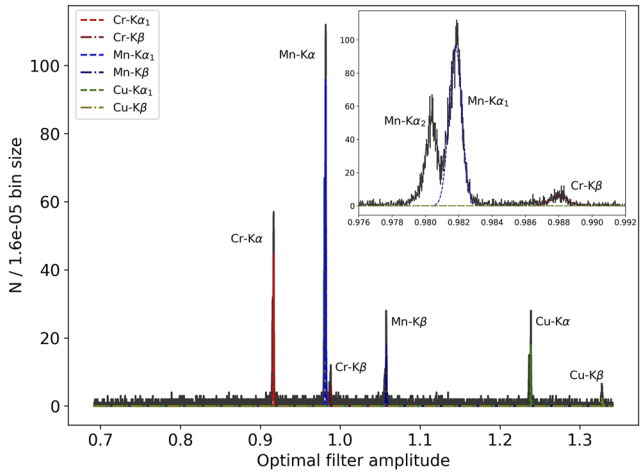

FIG. 5. Spectrum is obtained with a single pixel with the six calibration lines from the ^{55}Fe and MXS sources in about 2 h of data acquisition. The inset shows the detail of the Mn-Kα and Cr-Kβ lines. The optimal filter is constructed on the average photon energy of the ^{55}Fe source, weighted on the relative intensities of the Mn-Kα line complex and the Mn-Kβ line so that an optimal filter fit of 1 corresponds to an energy of 5957.29 eV.

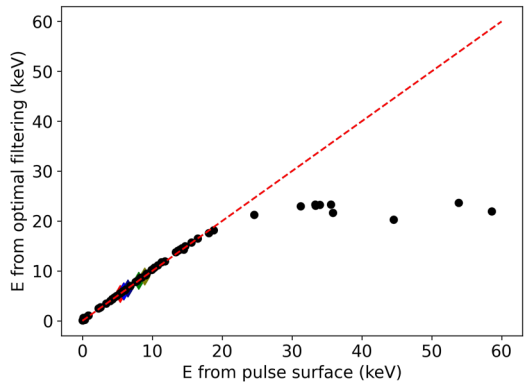

FIG. 6. Comparison of the pulse energy estimated with the optimal filter fit vs the energy estimated with the pulse area for one pixel. The correlation is linear up to ~15 keV, after which the energy estimated from the optimal filter fits becomes unreliable due to pulse saturation. The colored diamonds represent the position of the calibration lines, in the same color code as Fig. 5.

able to include pulses with larger energy than what was envisaged for this TES array in the analysis, although with a worse accuracy than with the optimal filter fits.

To do this, we first still calibrate the energy scale based on the optimal filter fits using the 0 energy information and the six spectral lines from the calibration sources. The calibration is performed using a 3rd order polynomial. We still keep the optimal filter fits as a reference since six spectral lines are identified with higher precision than with the pulse area. Then, we cross-correlate the spectrum calibrated in this way with the spectrum built using the pulse area of each event from the MXS-^{55}Fe calibration data. From the cross-correlated spectra in optimal filter fits and pulse area (see Fig. 7), we then get a one-to-one relationship between the surface and the energy. In this way, we obtain a pulse area-calibrated energy scale, allowing us to determine the energy of the background photons based on the pulse area. This technical issue would not be present, were we to use a TES array specifically designed with a larger dynamic range: in that case, the optimal filter fits would be used to estimate the energy of the pulses, granting better precision.

C. Data selection and baseline stability

Once the calibration of the energy scale is completed for each pixel, we proceed to analyze the data acquired in the period without a calibration source to study the background level in our experiment. To properly estimate the x-ray background, it is important to discern actual particles releasing energy in the TES absorber from events of different natures.

We do a first selection based on pulse polarity and time constants. We discard data with a surface of opposite sign and for which the fit for the rising and decay time constants failed, due to the rise and fall times being too fast or non-exponential. Such events are triggered by baseline drifts or spurious signals, such as electrical crosstalk.

Finally, we look at temporal coincidences between two or more events in different pixels to identify hits due to cosmic rays (high-energy muons). The effective active area is $S = 27 \times (240\ \mu\text{m})^2 \simeq 0.016\ \text{cm}^2$, with 27 being the number of pixels based on the working point. Given the approximate average muon flux at sea level of 1 muon per square centimeter per minute, the expected rate on the active detectors is about 1 muon per hour, with energies following a Landau distribution peaked at 7 keV, according to measurements with a cryogenic anti-coincidence in a similar FDM setup.[32] We are not able, however, to tag cosmic rays hitting only one pixel.

Another important factor to consider is that the detector response should be stable and insensitive to environmental disturbances, such as mechanical vibrations, thermal and electrical instabilities, and magnetic field fluctuations. In this regard, we recently reported on the susceptibility of the TES responsivity (or gain) under FDM readouts to such disturbances, demonstrating that their impact on the detector performance at the laboratory level is negligible, especially regarding magnetic fields.[33]

To estimate the detector stability during the long background data acquisitions (42 and 66 days), we consider the TES baseline current for each selected background event. The baseline is calculated via a linear fit of the TES current before and after the x-ray pulse (about 40 ms total temporal trace). For each regular pulse signal, the residual is then calculated as the normalized difference between the baseline of the event and the average baseline of all events for that pixel across the entire acquisition time.

Figure 8 shows the behavior of the baseline for each pixel during the background data acquisition. From the cumulative distribution of the residuals, we find that the TES stability over roughly 100 days of operation was at a level better than 1%. Note that this was obtained during the concurrent operation of three other cryogenic setups in the same refrigerator, which introduced some dead time in the measurement. These are the same conditions in which we typically perform experiments with x-ray sources to characterize the spectral performance of our detectors. In such experiments, a data acquisition run lasts a few hours; therefore, we do not

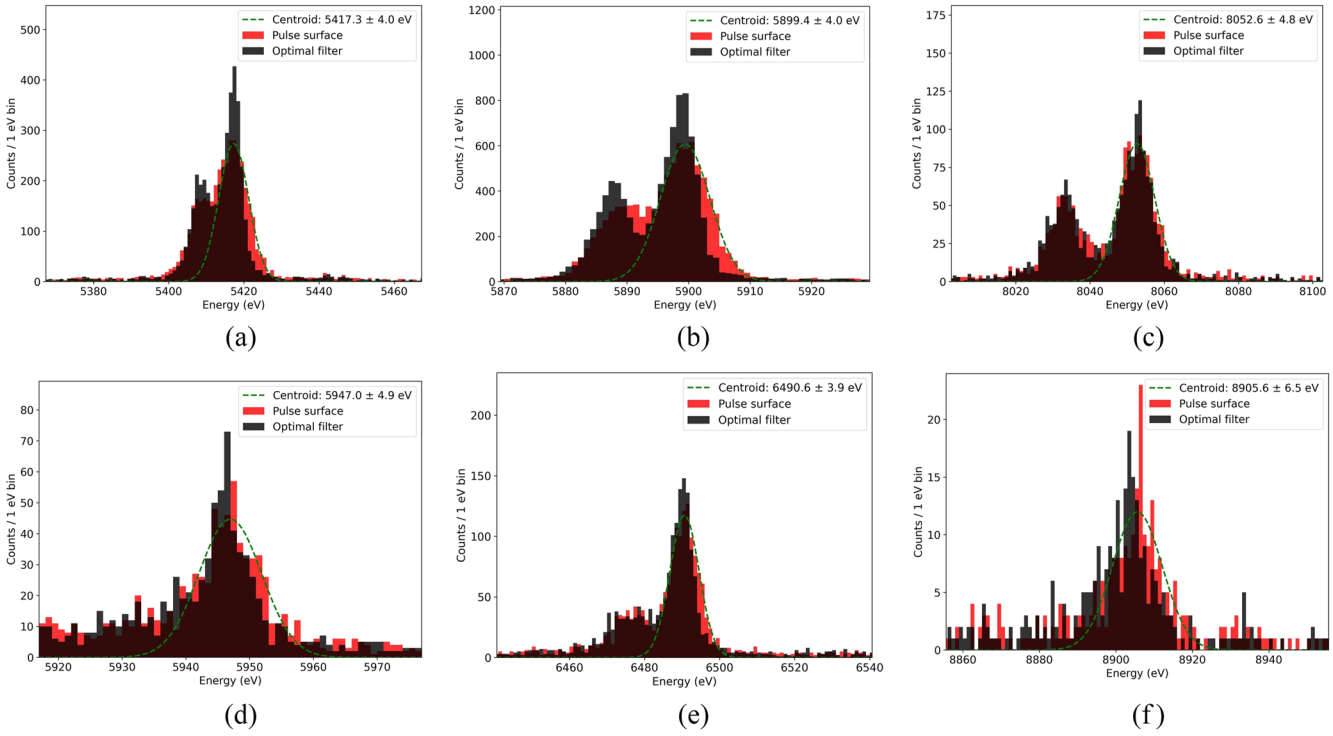

FIG. 7. Comparisons of spectral lines from the ^{55}Fe and MXS sources calibrated using the optimal filter fits (black) and the pulse surface (red), with the estimated Gaussian mean values from the fit of the pulse area histogram showed by the green dashed line. The reference values for the spectral lines[34] are (a) Cr-Kα_1: 5414.72 eV, (b) Mn-Kα_1: 5898.75 eV, (c) Cr-Kβ_1: 5946.71 eV, (d) Mn-Kβ_1: 6490.45 eV, (e) Cu-Kα_1: 8047.78 eV, and (f) Cu-Kβ_1: 8905.29 eV.

usually observe such long-scale baseline drifts. The baseline correction in the data analysis pipeline has been shown to correctly compensate for such drifts in the background events. As a result, the detectors' energy resolution is not significantly impacted by the 1% baseline instability. Nonetheless, we envisage that the TES stability would improve from this estimated level, were we to repeat this experiment in a dedicated refrigerator.

Before estimating the background from the histogram of the selected events, we correct for the detector's quantum efficiency. As we mentioned, this TES array is not optimized for this experiment, and the quantum efficiency is strongly non-linear above 6 keV, as shown in Fig. 9.

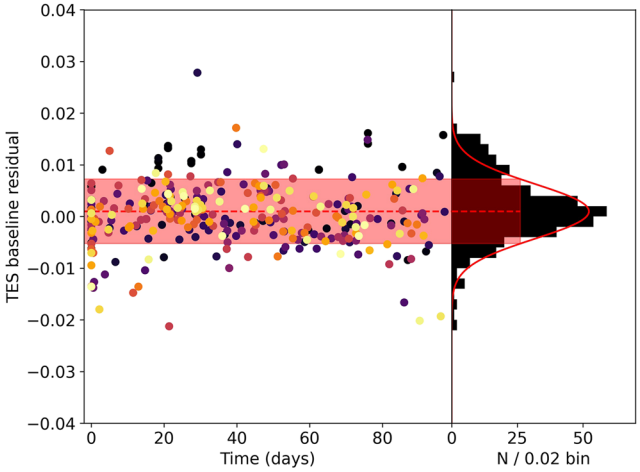

FIG. 8. Residuals of the TES baseline current as a function of data acquisition time (left) and cumulative histogram of the residuals (right). Each color corresponds to a different pixel. The cumulative distribution of the residuals is consistent with a Gaussian fit with a mean equal to 0.0004 and a FWHM equal to 0.0096.

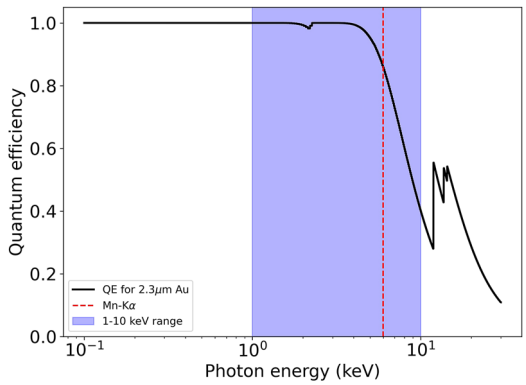

FIG. 9. Quantum efficiency for the 2.3 μm gold absorber. For 6 keV photons, the absorption probability is ~93%. Data are taken from Ref. 35.

V. RESULTS AND DISCUSSION

A. X-ray background without shielding

We performed a first acquisition run of $t \approx 42$ days. The histogram for the measured events is reported in Fig. 10(a). The background rate per bin is then estimated as

$$\frac{d\phi}{dE} = \frac{N_{bin}}{\delta E_{bin} S t}, \tag{6}$$

where N_{bin} is the number of events per bin, δE_{bin} is the bin energy width, and S is the effective active area. The error σ in each bin is given by the Poisson statistics as the square root of the bin counts. The error on the background rate per bin is then given in the same way, replacing Eq. (6) N_{bin} with its square root.

Since each bin gives an independent estimation of the background rate, we calculate it according to the maximum likelihood estimators,

$$\mu_{BG} = \frac{\sum_i N_i/\sigma_i^2}{\sum_i 1/\sigma_i^2}, \tag{7}$$

$$\sigma_{BG}^2 = \frac{1}{\sum_i 1/\sigma_i^2}. \tag{8}$$

To avoid underestimations, we use only the bins between 0.5 and 10 keV, the energy range where an ALP signal would be expected in an axion helioscope and where our TESs response is optimized. The background rate measured with this dataset is $1.24(5) \times 10^{-3}$ cm^{-2} s^{-1} keV^{-1}.

B. X-ray background with passive shielding

The measured level of x-ray background is expected to be arising from several contributions: cosmic rays (high-energy muons), γ-rays, neutrons, natural radioactivity, and cosmogenic activation of the materials constituting the cryogenic setup. These radioactive processes result in the production of secondary radiation (charged particles or fluorescence photons) that can reach the active detector area. Typical strategies to reduce the impact for each source include active shielding to veto cosmic ray events (plastic scintillators with high geometrical efficiency); high-Z materials (copper, lead) followed by plastic materials (PTFE, PMMA) to block γ-rays and the subsequent fluorescence photons, neutron moderation (e.g., via polyethylene, graphite), and subsequent absorption (typically via cadmium); and the use of radio-pure materials such as archeological leads.

In the successive cooling run, in an attempt to further reduce the background rate, we introduced a passive shielding scheme composed of a 2 mm thick Pb shield around the cryogenic setup (shown in Fig. 11), plus a 500 μm thick PTFE sheet inside the aluminum shell. Additionally, a 1 mm Kapton film is positioned right above the TES array, below the copper collimator. This was aimed mainly to reduce the impact of the fluorescence photons generated in the lead, aluminum, and copper and, in minor part, reduce the transmission of γ-rays. The Pb and PTFE shields have a full solid angle coverage, as they entirely surround the cryogenic setup and hence the detector array, contrarily to the Kapton layer that only covers the front side of the TES array chip. The screening efficiency of the Pb shield is expected to be larger than 99% for photons of energies below 150 keV, whereas the Teflon and Kapton are expected to absorb 90% of photons with energies below 7 and 6 keV, respectively.[35]

This shielding configuration has been constructed with materials immediately available in our laboratory, with the aim of performing a proof-of-concept experiment without a drastic redesign of the cryogenic assembly or the integration of an active shielding, which would have required several months.

Repeating the experiment with such makeshift passive shielding, we observed an improvement in the background rate, as shown in Fig. 10(b). In an effective data acquisition time of 66 days,

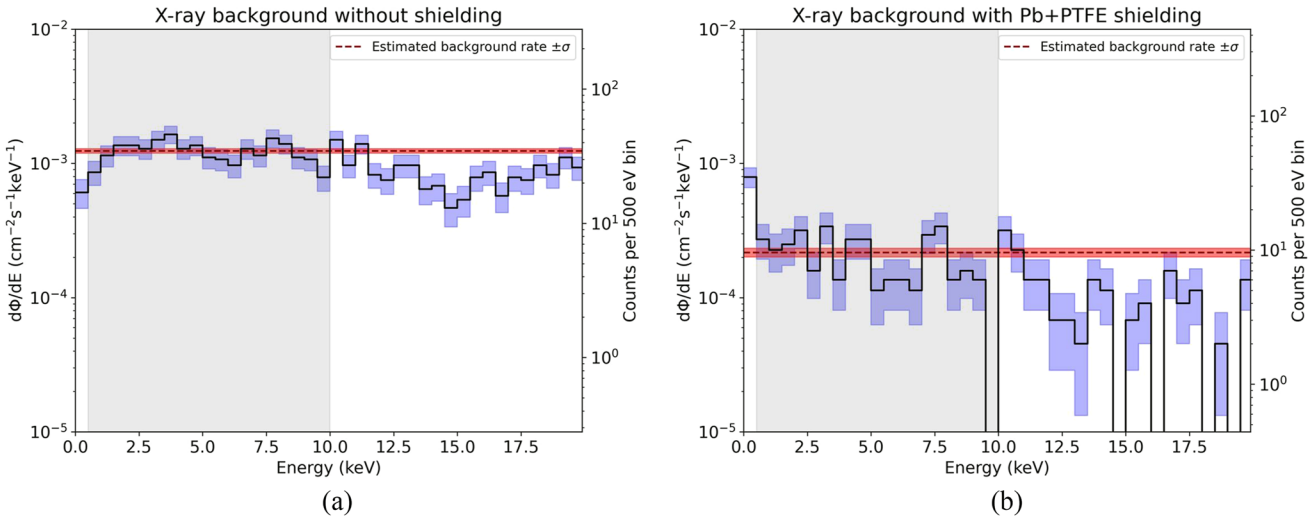

FIG. 10. The x-ray background rate was acquired without any shielding during 42 days of data acquisition time (a) and with Pb + PTFE shielding during 66 days of data acquisition (b). The gray area shows the 0.5–10 keV range used for the background estimation.

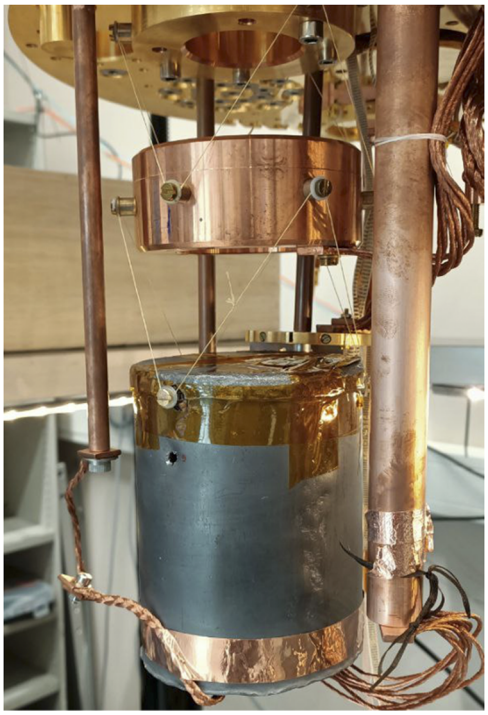

FIG. 11. Shield assembled with a 2 mm thick Pb sheet enclosing the setup to screen from background events external to the setup. To screen for fluorescence events generated in the lead and the inner Al shell, a 500 μm PTFE sheet is also implemented between the aluminum and the cryogenic components.

we measured a background rate of $2.2(2) \times 10^{-4}$ cm^{-2} s^{-1} keV^{-1}, i.e., an improvement of a factor ≈6, which could be explained as due to a reduction from the passive shielding of fluorescence photons impacting the TES absorbers, according to the expected x-ray absorption efficiencies discussed earlier.

C. Future outlook

The background rate measured with the passive shielding compares well with the $1.20(8) \times 10^{-4}$ cm^{-2} s^{-1} keV^{-1} recently reported for an array of MMCs optimized for IAXO,[36] as well as with the 1.5×10^{-4} cm^{-2} s^{-1} keV^{-1} initially demonstrated for Micromegas gaseous detectors,[37] before dedicated studies for reduction strategies allowed to reach the 6.6×10^{-7} cm^{-2} s^{-1} keV^{-1} demonstrated in CAST.[38]

This promising result motivates us to undertake a further effort to design and manufacture a new, dedicated setup for the demonstration of a background rate compliant with the requirements of rare event experiments such as IAXO, at a level of $<10^{-7}$ cm^{-2} s^{-1} keV^{-1}. In this section, we discuss several upgrades that might be implemented to achieve this goal.

A first major change would be to host the cryogenic assembly in an autonomous refrigerator, allowing for continuous operation and independence from disturbances arising from concurrent cryogenic experiments. This would avoid dead time during the data acquisition and improve the TES baseline stability.

The integration of an external active muon veto with plastic scintillators and large geometrical efficiency is expected to drastically improve the background rate. An alternative (or even concurrent) active shielding configuration to reduce the impact of cosmic rays would be a cryogenic anti-coincidence coupled to the TES array, *à la* Athena X-IFU,[39] which according to Geant4 simulations is expected to reduce the background rate up to a factor of 40.

Geant4 simulations are envisaged also to optimally design and dimension the cryogenic assembly and local passive shielding to mitigate the contribution of γ-rays and neutrons, with care in using radio-pure materials for the construction of the cryogenic assembly.

Both TES detectors and FDM readout characteristics would also need to be re-optimized. In SRON clean room facilities, the fabrication of a kilo-pixel TES array with bismuth absorbers with dimensions of the order of 1×1 mm^2 is achievable and would grant an active area at a level of 10 cm^2. The effective area can be further increased by using a multi-absorber TES scheme, also referred to as "hydra,"[40] e.g., by coupling nine absorbers with different G to the same TES and performing position identification from the pulse shape analysis.

The readout of one thousand detectors (or more if the hydra scheme would be employed) can be achieved via ten FDM channels, each reading out 100 TESs. This is viable if we assume the same current readout bandwidth in the 1 to 5 MHz range (although we expect a 1 to 6 MHz bandwidth to be also possible), using a spacing of 40 kHz between adjacent frequency channels and hence, for stability reasons, a gain-bandwidth product per pixel at a level of 6 kHz. This implies a maximum electrical bandwidth per pixel $1/\tau_{el} \equiv R/2\pi L$ of the order of 1 kHz, where R and L are the TES resistance at the working point and the inductance of the LC bandpass filter, respectively. Assuming a TES normal resistance of 200 mΩ and a working point from 10% to 20% of the superconducting transition, such as for SRON's 80×10 μm^2 pixel geometry, this implies the use of a ≈6 μH inductance, which is reasonably close the designs already available and could be easily achieved by replacing the transformer with one having the opportune coil ratio.

Moreover, in strong electro-thermal feedback operation, the electrical time constant τ_{el} poses the condition $\tau \gtrsim 5.8\tau_{el}$ on the TES effective time constant, defined in Eq. (4), to ensure electrical stability.[23] Consequently, the redesigned TES should be significantly slower than the current design, with an effective time constant at a level of 10 ms. Although this is not acceptable for x-ray astronomical observatories, this does not represent a problem for low-count rate experiments like axion helioscopes. Slower TESs can be engineered by increasing the heat capacity or reducing the thermal conductance. At low temperatures, the electron system dominates the heat capacity of the detector, which scales according to the formula,

$$C(T) = \frac{\rho}{A}\gamma VT, \tag{9}$$

with ρ, A, and γ being the material density, atomic number, and Sommerfeld constant, respectively, V is the volume, and T is the temperature. Therefore, increasing the active detector area to have higher count statistics for the background rate measurement also plays in favor of a larger time constant and a higher dynamic range.

However, the energy resolution scales with the square root of the heat capacity, according to Eq. (5). An increase in absorber area of factor 4 would then imply a degradation of factor 2 in energy

resolution to a level of ≈4 eV at 6 keV. Despite this being still acceptable for ALP search applications, other fundamental TES parameters could be tweaked to minimize the loss in energy resolution, such as the critical temperature. Such a study is currently undergoing and tests that will define the optimal TES geometry and FDM readout parameters are envisaged for the following years.

With these upgrades, assuming one thousand or more detectors for an effective active area of several cm^2, we expect to be able to measure an x-ray background rate for TES micro-calorimeters at a level better than 10^{-7} cm^{-2} s^{-1} keV^{-1} with one year of continuous data acquisition, thus demonstrating the feasibility of our TES-FDM technology for ALPs searches and axion helioscopes such as IAXO.

VI. SUMMARY

Axion-like particles (ALPs) are hypothetical pseudo-scalar particles representing an attractive dark matter candidate. A first solar ALPs detection at helioscopes requires x-ray detectors with high quantum efficiency and low background rate at levels less than 10^{-7} cm^{-2} s^{-1} keV^{-1}, whereas a high spectral performance is desirable to study axion physics. Transition-edge sensors (TES) fulfill such requirements and are thus a natural choice for ALPs search and axion helioscopes in particular.

We reported on the measurement of the background rate of a TES-based x-ray micro-calorimeter array readout under frequency-domain multiplexing. The TES array, the cryogenic assembly, and the test facility were developed and operated for experiments in the framework of Athena X-IFU and were not optimized for this application. We measured a background rate of $1.24(5) \times 10^{-3}$ cm^{-2} s^{-1} keV^{-1} with the bare setup during 42 days of data acquisition.

The implementation of a passive shielding with lead and PTFE in an attempt to reduce the contribution from γ radiation led to an improvement of the background rate down to $2.2(2) \times 10^{-4}$ cm^{-2} s^{-1} keV^{-1}. This value represents a promising starting point for a dedicated development, as it is comparable with the recent report for a metallic magnetic calorimeter array designed for IAXO and with the first background rate demonstrated in 2002 for the Micromegas gaseous detectors ultimately used for the CAST experiment.

To further improve the background rate to an acceptable level for future axion helioscopes, several upgrades are foreseen, including optimization of the TES and FDM readout characteristics and an improved shielding configuration via active muon veto (plastic scintillators and/or cryogenic anti-coincidence) and Geant4-aided design of the passive shielding and the cryogenic assembly, which should be composed of radio-pure materials and housed in an independent cryostat.

We expect that such improvements would allow us to reach a background rate $\leq 10^{-7}$ cm^{-2} s^{-1} keV^{-1} with one year of data acquisition.

ACKNOWLEDGMENTS

SRON was financially supported by the Nederlandse Organisatie voor Wetenschappelijk Onderzoek.

This work was part of the research program Athena with Project No. 184.034.002, which is (partially) financed by the Dutch Research Council (NWO).

The SRON TES arrays used for the measurements reported in this paper is developed in the framework of the ESA/CTP Grant No. ITT AO/1-7947/14/NL/BW.

AUTHOR DECLARATIONS

Conflict of Interest

The authors have no conflicts to disclose.

Author Contributions

D. Vaccaro: Conceptualization (equal); Data curation (lead); Formal analysis (lead); Methodology (equal); Software (lead); Writing – original draft (lead); Writing – review & editing (lead). **L. Gottardi**: Conceptualization (equal); Formal analysis (supporting); Methodology (equal); Writing – review & editing (equal). **H. Akamatsu**: Formal analysis (supporting); Writing – review & editing (equal). **J. van der Kuur**: Writing – review & editing (supporting). **K. Nagayoshi**: Writing – review & editing (supporting). **E. Taralli**: Writing – review & editing (equal). **M. de Wit**: Writing – review & editing (equal). **K. Ravensberg**: Writing – review & editing (supporting). **J. R. Gao**: Writing – review & editing (supporting). **J. W. A. den Herder**: Writing – review & editing (supporting).

DATA AVAILABILITY

The corresponding author makes available the data presented in this paper upon reasonable request.

REFERENCES

[1] S. Kempf, A. Fleischmann, L. Gastaldo, and C. Enss, "Physics and applications of metallic magnetic calorimeters," J. Low Temp. Phys. **193**, 365–379 (2018).

[2] L. Gottardi and K. Nagayashi, "A review of x-ray microcalorimeters based on superconducting transition edge sensors for astrophysics and particle physics," Appl. Sci. **11**(9), 3793 (2021).

[3] D. Barret, V. Albouys, J.-W. den Herder, L. Piro, M. Cappi, J. Huovelin, R. Kelley, J. M. Mas-Hesse, S. Paltani, G. Rauw *et al.*, "The Athena x-ray integral field unit: a consolidated design for the system requirement review of the preliminary definition phase," in *Experimental Astronomy* (Springer, 2023).

[4] W. Cui, L.-B. Chen, B. Gao, F.-L. Guo, H. Jin, G.-L. Wang, L. Wang, J.-J. Wang, W. Wang, Z.-S. Wang *et al.*, "HUBS: Hot universe baryon surveyor," J. Low Temp. Phys. **199**, 502–509 (2020).

[5] M. Hazumi, P. A. R. Ade, A. Adler, E. Allys, K. Arnold, D. Auguste, J. Aumont, R. Aurlien, J. Austermann, C. Baccigalupi *et al.*, "LiteBIRD: JAXA's new strategic L-class mission for all-sky surveys of cosmic microwave background polarization," Proc. SPIE **11443**, 114432F (2020).

[6] J. Rothe, G. Angloher, P. Bauer, A. Bento, C. Bucci, L. Canonica, A. D'Addabbo, X. Defay, A. Erb, F. v. Feilitzsch *et al.*, "TES-based light detectors for the CRESST direct dark matter search," J. Low Temp. Phys. **193**, 1160–1166 (2019).

[7] B. Alpert, M. Balata, D. Bennett, M. Biasotti, C. Boragno, C. Brofferio, V. Ceriale, D. Corsini, P. K. Day, M. De Gerone *et al.*, "HOLMES: The electron capture decay of ^{163}Ho to measure the electron neutrino mass with sub-eV sensitivity," Eur. Phys. J. C **75**, 112 (2015).

[8] M. Beretta and L. Pagnanini, "Development of cryogenic detectors for neutrinoless double beta decay searches with CUORE and CUPID," Appl. Sci. **11**, 1606 (2021).

[9] M. E. Eckart, P. Beiersdorfer, G. V. Brown, D. J. Den Hartog, N. Hell, R. L. Kelley, C. A. Kilbourne, E. W. Magee, A.-E. Y. Mangoba, M. D. Nornberg

et al., "Microcalorimeter measurement of x-ray spectra from a high-temperature magnetically confined plasma," Rev. Sci. Instrum. **92**, 063520 (2021).
[10]M. R. J. Palosaari, K. M. Kinnunen, J. Julin, M. Laitinen, M. Napari, T. Sajavaara, W. B. Doriese, J. Fowler, C. Reintsema, D. Swetz *et al.*, "Transition-edge sensors for particle induced x-ray emission measurements," J. Low Temp. Phys. **176**, 285–290 (2014).
[11]R. Shah, K.-S. Isleif, F. Januschek, A. Lindner, and M. Schott, "Characterizing a single-photon detector for ALPS II," J. Low Temp. Phys. **209**, 355 (2022).
[12]R. D. Peccei and H. R. Quinn, "CP conservation in the presence of pseudoparticles," Phys. Rev. Lett. **38**, 1440 (1977).
[13]J. Preskill, M. B. Wise, and F. Wilczek, "Cosmology of the invisible axion," Phys. Lett. **120**, 127 (1983).
[14]P. Sikivie, "Experimental tests of the invisible axion," Phys. Rev. Lett. **51**, 1415 (1983).
[15]S. Moriyama, M. Minowa, T. Namba, Y. Inoue, Y. Takasua, and A. Yamamoto, "Direct search for solar axions by using strong magnetic field and x-ray detectors," Phys. Lett. B **434**, 147 (1998).
[16]C. A. J. O'Hare, A. Caputo, A. J. Millar, and E. Vitagliano, "Axion helioscopes as solar magnetometers," Phys. Rev. D **102**, 043019 (2020).
[17]V. Anastassopoulos, S. Aune, K. Barth, A. Belov, H. Brauninger, G. Cantatore, J. M. Carmona, J. F. Castel, S. A. Cetin, F. Christensen *et al.*, "New CAST limit on the axion–photon interaction," Nat. Phys. **13**, 584–590 (2017).
[18]E. Armengaud, D. Attie', S. Basso, P. Brun, N. Bykovskiy, J. M. Carmona, J. F. Castel, S. Cebrian, M. Cicoli, M. Civitani *et al.*, "Physics potential of the international axion observatory (IAXO)," J. Cosmol. Astropart. Phys. **2019**, 047.
[19]K. Altenmüllera, B. Biasuzzic, J. F. Castela, S. Cebriána, T. Dafnia, K. Deschd, D. Díez-Ibañeza, E. Ferrer-Ribasc, J. Galana, and J. Galindo, *X-Ray Detectors for the BabyIAXO Solar Axion Search* (NIMA, Elsevier, 2023), p. 1048167913.
[20]J. Jaeckel and L. J. Thormaehlen, "Axions as a probe of solar metals," Phys. Rev. D **100**, 123020 (2019).
[21]F. M. Brunbauer, D. Desforge, E. Ferrer-Ribas, F. J. Iguaz, B. Mehl, R. De Oliveira, E. Oliveri, T. Papaevangelou, O. Pizzirusso, E. C. Pollacco *et al.*, "Radiation imaging with glass Micromegas," Nucl. Instrum. Methods Phys. Res., Sect. A, **955** 163320 (2020).
[22]M. de Wit, L. Gottardi, K. Nagayoshi, H. Akamatsu, M. P. Bruijn, M. L. Ridder, E. Taralli, D. Vaccaro, J.-R. Gao, and J. W. A. den Herder, "Performance of the SRON Ti/Au transition edge sensor x-ray calorimeters," Proc. SPIE **12181**, 121812B (2022).
[23]K. D. Irwin, G. C. Hilton, D. A. Wollman, and J. M. Martinis, "Thermal-response time of superconducting transition-edge microcalorimeters," J. Appl. Phys. **83**, 3978 (1998).
[24]K. Nagayoshi, M. L. Ridder, M. P. Bruijn, L. Gottardi, E. Taralli, P. Khosropanah, H. Akamatsu, S. Visser, and J.-R. Gao, "Development of a Ti/Au TES microcalorimeter array as a backup sensor for the Athena/X-IFU instrument," J. Low Temp. Phys. **199**, 943–948 (2020).
[25]W. B. Doriese, K. M. Morgan, D. A. Bennett, E. V. Denison, C. P. Fitzgerald, J. W. Fowler, J. D. Gard, J. P. Hays-Wehle, G. C. Hilton, and K. D. Irwin, "Developments in time-division multiplexing of x-ray transition-edge sensors," J. Low Temp. Phys. **184**, 389–395 (2016).
[26]H. Akamatsu, L. Gottardi, J. van der Kuur, C. P. de Vries, M. P. Bruijn, J. A. Chervenak, M. Kiviranta, A. J. van den Linden, B. D. Jackson, A. Miniussi *et al.*, "Progress in the development of frequency-domain multiplexing for the x-ray integral field unit on board the Athena mission," J. Low Temp. Phys. **199**(3-4), 737–744 (2020).
[27]R. den Hartog, D. Boersma, M. Bruijn, B. Dirks, L. Gottardi, H. Hoevers, R. Hou, M. Kiviranta, P. de Korte, J. van der Kuur *et al.*, "Baseband feedback for frequency domain multiplexed readout of TES x-ray detectors," API Conf. Proc. **1185**, 261 (2009).
[28]H. Akamatsu, D. Vaccaro, L. Gottardi, J. van der Kuur, C. P. de Vries, M. Kiviranta, K. Ravensberg, M. D'Andrea, E. Taralli, M. de Wit *et al.*, "Demonstration of MHz frequency domain multiplexing readout of 37 transition edge sensors for high-resolution x-ray imaging spectrometers," Appl. Phys. Lett. **119**, 182601 (2021).
[29]See https://www.vttresearch.com/en for information about services and infrastructures.
[30]L. Gottardi, H. van Weers, J. Dercksen, H. Akamatsu, M. P. Bruijn, J. R. Gao, B. Jackson, P. Khosropanah, J. van der Kuur, K. Ravensberg, and M. L. Ridder, "A six-degree-of-freedom micro-vibration acoustic isolator for low-temperature radiation detectors based on superconducting transition-edge sensors," Rev. Sci. Instrum. **90**, 055107 (2019).
[31]A. E. Szymkowiak, R. L. Kelley, S. H. Moseley, and C. K. Stahle, "Signal processing for micro-calorimeters," J. Low Temp. Phys. **93**, 281–285 (1993).
[32]M. D'Andrea, K. Ravensberg, A. Argan, D. Brienza, S. Lotti, C. Macculi, G. Minervini, L. Piro, G. Torrioli, F. Chiarello *et al.*, "ATHENA X-IFU demonstration model: First joint operation of the main TES array and its cryogenic anticoincidence detector (CryoAC)," J. Low Temp. Phys. **209**, 433–440 (2022).
[33]D. Vaccaro, H. Akamatsu, L. Gottardi, J. van der Kuur, E. Taralli, M. de Wit, M. P. Bruijn, R. den Hartog, M. Kiviranta, A. J. van der Linden *et al.*, "Susceptibility study of TES micro-calorimeters for x-ray spectroscopy under FDM readout," J. Low Temp. Phys. **209**, 562–569 (2022).
[34]G. Hölzer, M. Fritsch, M. Deutsch, J. Härtwig, and E. Förster, "$K\alpha_{1,2}$ and $K\beta_{1,3}$ x-ray emission lines of the 3*d* transition metals," Phys. Rev. A **56**(6), 4554 (1997).
[35]See https://henke.lbl.gov/optical_constants/filter2.html for to reproduce the calculation.
[36]D. Unger, A. Abeln, C. Enss, A. Fleischmann, D. Hengstler, S. Kempf, and L. Gastaldo, "High-resolution for IAXO: MMC-based x-ray detectors," J. Instrum. **16**, P06006 (2021).
[37]J. G. Garza, S. Aune, F. Aznar, D. Calvet, J. F. Castel, F. E. Christensen, T. Dafni, M. Davenport, T. Decker, E. Ferrer-Ribas *et al.*, "Low background Micromegas in CAST," J. Phys.: Conf. Ser. **650**, 012008 (2015).
[38]S. Aune, F. Aznar, D. Calvet, T. Dafni, A. Diago, F. Druillole, G. Fanourakis, E. Ferrer-Ribas, J. Galán, and J. A. García, "X-ray detection with Micromegas with background levels below 10^{-6} cm^{-2} s^{-1} keV^{-1}," J. Instrum. **8**, C12042 (2013).
[39]C. Macculi, A. Argan, D. Brienza, M. D'Andrea, S. Lotti, G. Minervini, L. Piro, M. Biasotti, L. Ferrari Barusso, and F. Gatti, "The cryogenic anticoincidence detector for ATHENA X-IFU: The project status," J. Low Temp. Phys. **199**, 416–424 (2020).
[40]S. J. Smith, J. S. Adams, S. R. Bandler, J. A. Chervenak, A. M. Datesman, M. E. Eckart, F. M. Finkbeiner, R. Hummatov, R. L. Kelley, C. A. Kilbourne *et al.*, "Multiabsorber transition-edge sensors for x-ray astronomy," J. Astron. Telesc. Instrum. Syst. **5**(Issue 2), 021008 (2019).